B. Poole, A. Marsh, D. Lunt, C. Hardie, M. Gorley, C. Hamelin, A. Harte

High resolution strain mapping in a thermionic LaB6 SEM

High resolution strain mapping in a thermionic LaB6 SEM

B. Poole, A. Marsh, D. Lunt, C. Hardie, M. Gorley, C. Hamelin, A. Harte

High resolution strain mapping in a thermionic LaB$_6$ SEM

Benjamin Poole[1], Alex Marsh[1], David Lunt[1,2], Chris Hardie[1], Mike Gorley[1], Cory Hamelin[1], Allan Harte[1]

[1] United Kingdom Atomic Energy Authority, Culham Centre for Fusion Energy, Culham Science Centre, Abingdon, Oxon, OX14 3DB, UK
[2] Department of Materials, University of Manchester, Manchester, M13 9PL, UK

1   ABSTRACT

The high source stability and brightness of field emission gun equipped scanning electron microscopes (SEM) makes them ideal for high-resolution digital image correlation (HRDIC). However, their high initial capital cost can be prohibitive for research organisations and groups. Conventional thermionic SEMs using either a tungsten hairpin or LaB$_6$ filament are far more widespread due to their lower cost. Whilst it is understood that overall performance and ultimate resolution are lower than field emission SEMs, we propose that there is no fundamental reason why these instruments are unsuitable for HRDIC. We investigate the use of a LaB$_6$ SEM as a viable tool for HRDIC. We detail the subtleties of performing HRDIC using a LaB$_6$ thermionic source SEM, providing technical recommendations for best practices in using these instruments for strain mapping. The effects of instrument parameters on strain measurement noise are examined, with a focus on parameters of key relevance to in-situ and ex-situ mechanical testing. Errors in focus and magnification are found to be the primary contributors to the strain noise floor values, with stage accuracy being of secondary importance. We present a case study in oxygen-free high-conductivity copper, OFHC-Cu, which is used in the designs of nuclear fusion components as a heat sink interlayer. Heterogeneous strain patterns are observed in this material, with high levels of strain localisation at grain boundaries. Active slip systems are identified using the relative displacement ratio method, demonstrating the quality of these data and the suitability of LaB$_6$ instruments for HRDIC strain mapping, achieving performance approaching that expected of a field emission SEM.

2   INTRODUCTION

High-resolution digital image correlation (HRDIC) has reached a high level of maturity over the last decade, where large area, highly spatially resolved strain and displacement measurements can be captured using a suitably patterned specimen, the application of deformation and careful imaging with a scanning electron microscope. Typically, a field emission scanning electron microscope (FESEM) is used to capture the pre- and post-deformation images for HRDIC analyses due to their superior resolving power, source brightness and beam stability. However, these instruments are costly to purchase and operate, somewhat limiting their availability. Conventional SEMs which use a tungsten or LaB$_6$ emitter are significantly less expensive and require lower levels of maintenance and are, therefore, often used as analysis workhorses in industrial research and quality control laboratories.

There is a general drive for industrial acceptance of optical DIC for full-field deformation and displacement measurement through standardisation [1]. Optical DIC is a much more mature technique than SEM-based HRDIC, where fully off-the-shelf commercial solutions exist for the former. As a technique, HRDIC is still far from standardisation due to the small (but growing) number of users. Enabling the use of HRDIC in conventional SEMs is another step towards facilitating more widespread use of the technique. As far as we are aware, there are

no accounts of the use of conventional, thermionic SEMs for full-field strain mapping in the open literature.

Significant efforts have been made to understand the use of FESEMs for HRDIC measurements and optimising experimental procedures. Much of this work has focused on characterising the effect of various imaging artefacts and suggesting methods to improve them. These studies employ a range of techniques to ameliorate the effect of artefacts in strain maps using improved experimental procedures, additional SEM hardware, or with post-processing routines. Mello et al. [2] suggest the use of calibrated etched silicon grid specimens to correct for spurious displacements due to errors in the SEM scan path, applying the distortion field calculated from the known silicon grid specimen to DIC strain maps captured during real experiments. Other examples of similar post-processing distortion corrections with varying levels of complexity exist in the literature (e.g. [3–5]). External scan generators have been employed to better control the position of the electron beam during scanning, utilising a snake scan rather than a typical raster scan [6,7]. Unfortunately, the use of this highly specialist equipment further reduces the ease of adoption of HRDIC as a routine technique.

To ascertain whether conventional SEMs are suitable for full-field strain mapping, we examine the behaviour of a LaB_6 SEM for capturing images for HRDIC and perform a systematic study on key operating parameters which are likely to influence results in both in-situ and ex-situ mechanical testing. We also provide some best practice guidance for the use of LaB_6 SEMs. We perform a case study on OFHC-Cu, mapping deformation and linking strain distributions to electron backscatter diffraction orientation measurements. To verify the quality of the results, we perform relative displacement ratio analysis [8] over a range of grains which display differing slip characteristics. The success of this study demonstrates the viability of using this type of instrument for micromechanical experiments, enabling this technique for a wider range of users.

3   OPERATING CONDITIONS

As far as we are aware, HRDIC has thus far only been applied with FESEM instruments. Schottky field emitters appear to be the most popular field emission source type due to their high beam stability unlike Cold field emission guns which require flashing to maintain a clean filament tip. However, there is no fundamental limitation to thermionic LaB_6 source SEMs which would make these instruments unsuitable for HRDIC. The key attributes which make an instrument capable of HRDIC strain measurement are sufficient imaging resolution to image the speckles, suitable detectors to capture the images, and sufficient stability in the electron optics to ensure consistent imaging conditions.

Although field emitters offer superior ultimate resolution, LaB_6 sources are comparable to FE sources in terms of source stability [9]. To examine a statistical number of grains, large area images are required at high spatial resolution. Due to the relatively slow imaging rate of SEMs, individual images taken at a typical field width of tens of microns can take approximately one minute to capture. For a large total area of interest, several hundred microns wide, a complete imaging run can take several hours. Therefore, a stable beam and column are necessary to ensure consistent imaging throughout a run where a montage of hundreds of images is captured. Recently, studies have been conducted with single deformation steps containing over 400 images (both in-situ and ex-situ) and this desire for larger datasets is likely to increase further [10].

External diode-type backscattered electron (BSE) detectors are typically used for HRDIC using gold-remodelled patterns (e.g. [11–13]) due to their large collection solid angle and high sensitivity. Imaging using BSEs allows us to take advantage of the high levels of contrast generated by the difference in atomic number between thin film remodelled speckle

patterns and the substrate. These detectors are readily found on many thermionic SEMs. A Zeiss EVO 10 LaB$_6$ SEM is used as the test instrument for this study, representing a relatively conventional materials characterisation instrument, typical of those found in many engineering laboratories. This SEM fulfils the herein described features necessary for HRDIC.

An oxygen-free high-conductivity copper (OFHC-Cu) specimen was used in this study, using the method described in [14] to produce a speckle pattern suitable for HRDIC. Layers of titanium (3 nm) and silver (5 nm) were sputtered onto the specimen surface. The silver film was then remodelled in a 1 wt.% NaBr in isopropanol solution for 2 hours, resulting in a fine dispersion of ~ 80 nm speckles.

As a starting point, we attempted to take HRDIC-suitable images using the parameters typically used in FESEM instruments. These are low accelerating voltages to minimise orientation contrast from the substrate, moderate beam currents (~1 nA) to reduce scanning times, and short working distances to maximise both the spatial resolution and the signal to noise ratio [11]. Low accelerating voltages enhance surface information by reducing the beam interaction volume, maximising the surface signal contribution. For FESEMs, the electron probe diameter is generally always smaller than the effective image pixel size, even at low voltages. However, for thermionic emitters, there is a significant dependence of probe diameter on the accelerating voltage, with low voltages limiting the spatial resolution [9]. The backscatter coefficient has no strong dependence on beam energy and therefore the accelerating voltage can be chosen to maximise signal-to-noise ratio and spatial resolution [9].

The probe current directly affects the probe diameter, with an approximately linear relationship between diameter and current for currents exceeding 100 pA in thermionic SEMs [9]. Lower probe currents require longer pixel dwell times to give sufficient signal-to-noise ratios. However, long dwell times are known to increase the uncertainty in strain measurement with HRDIC due to increasing sample charging and drift [2,6]. There is also the practical limit of longer frame times extending the time required to image the region of interest for each strain step. For in-situ experiments, this can reduce the number of strain steps possible in a given time and can introduce unintentional creep holds where the specimen may be held under load for long periods.

For this work, an accelerating voltage of 20 kV and a probe current of 1 nA were selected as a balance between beam penetration, spatial resolution and imaging time. The 20 kV accelerating voltage has the benefit of offering enhanced subsurface grain contrast over lower accelerating voltages. This contrast is useful when aligning HRDIC and EBSD maps. A 20 μm column aperture was found to offer the highest quality images and highest level of image stability. A pole-piece mounted, four quadrant backscatter detector was used to capture images with the gain set to high. Brightness and contrast were set manually to give bright speckles on a dark background, minimising topology and orientation contrast as far as possible. A working distance of 5.5 mm was used throughout to maximise the BSE signal. For subsequent deformation steps, the best effort was made to match the contrast and brightness of the initial image.
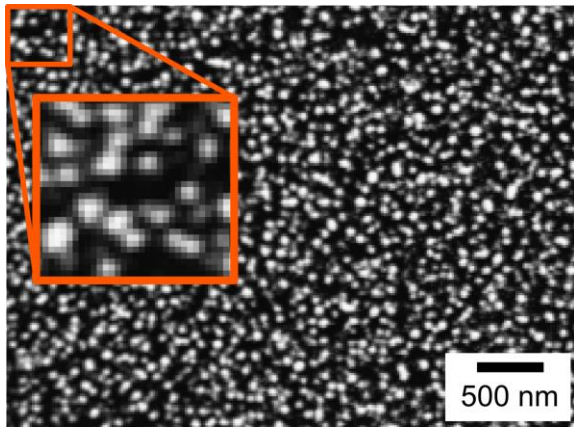
Figure 1: Subset of an optimised image for HRDIC. The highlighted region is magnified to show the pixel level detail with a 17 nm pixel size. The pattern here is generated from a 5 nm silver film.

The speckle pattern determines the individual tile field width to ensure that each speckle contains a sufficient number of pixels, with a minimum of 3-5 pixels for each speckle [1]. However, we found that setting the image magnification to achieve this criterion has a deleterious effect on image noise. Images taken at this scale required prohibitively long pixel dwell times (in excess of 100 µs) to achieve stable and consistent images. This is likely to be due to the limitations of the spot size of the SEM with respect to the speckle size, something not encountered with a FESEM. Individual tiles with horizontal field widths of 35 µm were found to offer sufficient imaging stability at reasonable dwell times and satisfy the pixel size requirements for DIC. A pixel dwell time of 10 µs with a frame resolution of 2048 × 1536 pixels gave a frame time of approximately 35 s. This allows a 10 × 10 grid of images to be captured in under an hour. Figure 1 shows a BSE image optimised for DIC demonstrating a high level of contrast between the substrate and speckles with the magnification set to ensure sufficient pixels per speckle.

4   SEM PERFORMANCE AND ERROR QUANTIFICATION

Since DIC provides quantitative displacement and strain measurements, it is necessary to quantify the errors due to instrument conditions. Significant efforts exist within the optical DIC community in increasing the reproducibility of DIC strain measurements through the publication of best practice guides and recommendations for reporting DIC data [1]. SEM-based HRDIC is a much newer technique and, as such, the errors are less well quantified and generally not reported. Some effort has been made to measure the errors associated with SEM-based imaging, quantifying distortions due to various imaging conditions [2,5,6] but this is currently not widespread.

In this study, we present a series of tests to quantify errors due to basic SEM parameters which may be inadvertently perturbed during experiments. We examine the sensitivity of strain measurement to stage accuracy and reproducibility, errors in focus and errors in magnification. Since measures of strain and displacement are distributions rather than single values, all data are presented as box plots showing the median at the centre, the interquartile range as the width of the box and the upper and lower quartiles plus/minus 1.5 times the interquartile range as the limits of the whiskers.

4.1   Image correlation

A pair of 35 µm field width images were used to assess the noise for each system perturbation. Images were correlated using LaVision DaVis 10.0.5 with a decreasing window FFT algorithm. The FFT algorithm was selected over the default least squares matching algorithm within DaVis as it offers superior performance for the discontinuous deformation

fields observed in metal plasticity [15]. A coarse image alignment was performed on the raw images using ImageJ to remove some rigid body motion between images. A second combined shift and rotation correction was performed in DaVis, followed by image correlation. All data post processing and manipulation were performed using the DefDAP python package [16] and with additional in-house python routines. Raw pixel displacements, u_1 and u_2 in the in-plane directions x_1 and x_2 respectively, were exported from DaVis with strains calculated using DefDAP. The in-plane deformation gradient could then be calculated.

$$\nabla \mathbf{u} = \begin{pmatrix} \dfrac{\partial u_1}{\partial x_1} & \dfrac{\partial u_2}{\partial x_1} \\ \dfrac{\partial u_1}{\partial x_2} & \dfrac{\partial u_2}{\partial x_2} \end{pmatrix}$$

(1)

For metallic systems, crystallographic slip is the primary deformation mechanism. Since this is a shear dominated mechanism, the maximum in-plane shear strain is the most suitable strain measure. For simplicity we call this the effective strain, E_{eff}.

(2)

$$E_{\text{eff}} = \sqrt{\left(\frac{\frac{\partial u_1}{\partial x_1} - \frac{\partial u_2}{\partial x_2}}{2} \right)^2 + \left(\frac{\frac{\partial u_1}{\partial x_2} + \frac{\partial u_2}{\partial x_1}}{2} \right)^2}$$

Individual strain components are defined as $E_{11} = \frac{\partial u_1}{\partial x_1}$, $E_{22} = \frac{\partial u_2}{\partial x_2}$ and $E_{12} = \frac{1}{2}\left(\frac{\partial u_1}{\partial x_2} + \frac{\partial u_2}{\partial x_1} \right)$.

The decreasing window FFT cross-correlation used an initial 1024 px × 1024 px subset, reducing for successive passes. The ultimate cross-correlation subset size was optimised by finding the noise level as a function of subset, correlating pairs of images taken sequentially without any changes to the system. The optimal subset size was taken at the point where the maximum in-plane shear strain E_{eff} exceeded an acceptable noise level, taken as 1%. This 1% value is typical of the noise levels encountered in the literature [15,17] and is well below the strains of associated with strain localisation. A 50% subset overlap was used for all measurements to increase the correlation accuracy, as the particle spacing was larger than a single particle diameter. An optimal subset size of 16 px × 16 px was determined for these images, balancing spatial resolution against noise (Figure 2). This optimal subset size was used for all error analysis testing. This results in a final spatial resolution in the strain maps of 136 nm.
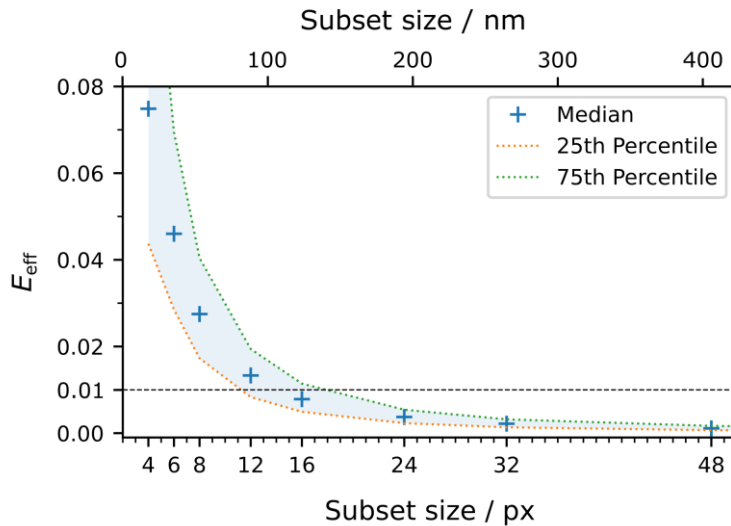
Figure 2: Maximum in-plane shear strain E_{eff} as a function of cross-correlation subset size, showing the 25th and 75th percentiles in strain values.

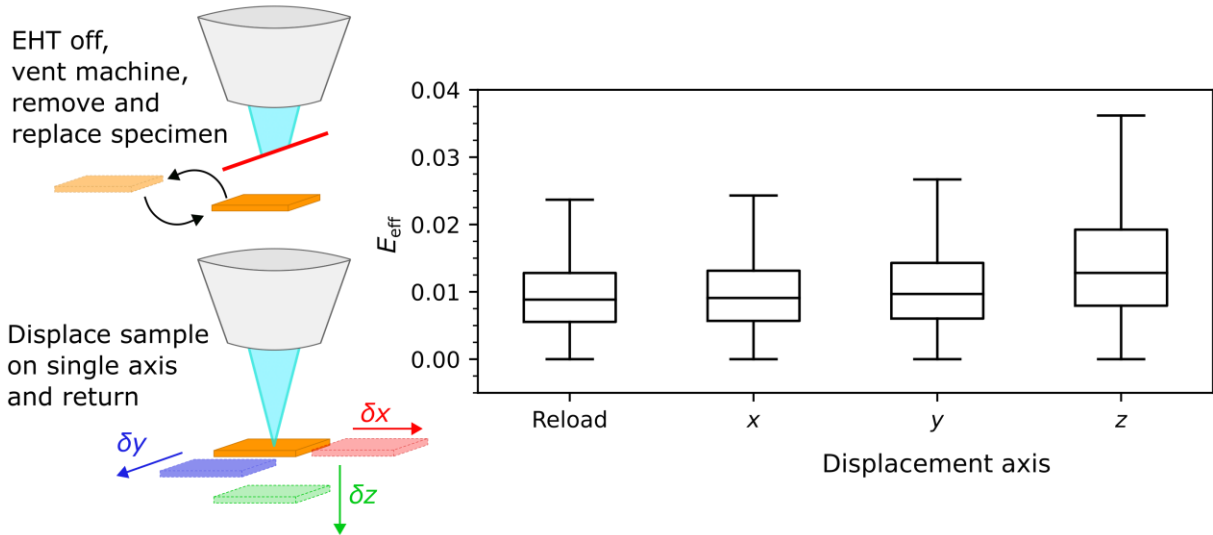## 4.2 Sensitivity to stage motion

Since stage position automation is often used to capture large grids of images to increase the size of the region of interest (ROI), it is important to measure the influence of uncertainties in stage position. In these tests we simulate both the effects of stage motion in the SEM, representative of in-situ testing and large area mapping, and the effect of removing and reloading the specimen which replicates an ex-situ test.

For the reload test, the electron beam was switched off, the chamber vented, and the specimen removed from the stage. The process was then reversed to reload the specimen and the ROI found with fiducial markers using a combination of *x* and *y* stage motion. For the *x*, *y* and *z* stage motion tests, a reference image was captured, the specimen displaced 100 μm in the positive direction and then 100 μm in the negative direction to return the stage to the nominal initial position. A second image was then captured and correlated against the reference image to measure the systematic error due to stage motion. Stage rotation was also tested, applying a 10° rotation and return. The stage was so inaccurate in the rotation axis that the ROI had moved out of view when the stage was returned to the nominal initial position. As such, we strongly recommend against using stage rotation during automated image capture.
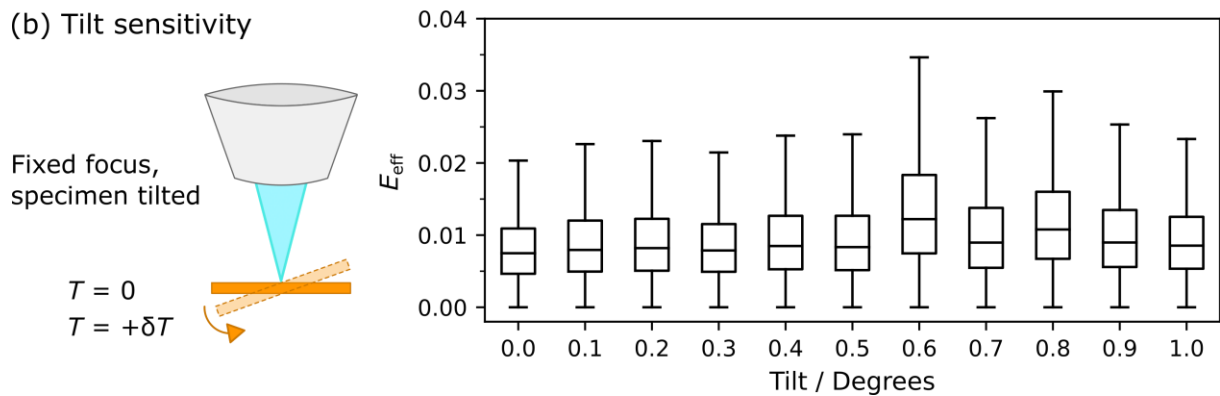
Sensitivity to out-of-plane tilt was examined by taking a pre-motion reference image and then tilting the specimen in 0.1° increments up to 1° tilt. The focal point was not adjusted. The centre of the ROI was brought back into position with *x* and *y* stage motion with focus at the ROI centre achieved by manually adjusting the stage *z* position.

As shown in Figure 3a, values of E_{eff} were largely insensitive to all stage motion with median strain values of approximately 1% for all tests. A slight increase in noise was observed for the *z*-displacement test due to a small change in focus. In contrast, tilt (Figure 3b) exhibited a higher degree of variation but this was still within an acceptable level of absolute noise. The variation was likely caused by the manual refocussing of the image using the stage *z* position. These focussing effects are explored further in Section 4.3. These results demonstrate that the *z*-axis of stage motion is the key control parameter to reduce noise in HRDIC-based strain measurement, outweighing contributions from *x* and *y* position inaccuracies. It is also encouraging to see that a full specimen reload cycle does not introduce significant error into measurements. For a multi-stage ex-situ deformation experiment using an external loading frame, a specimen will be loaded and removed from the SEM multiple times.

(a) x,y, z sensitivity

EHT off,
vent machine,
remove and
replace specimen

Displace sample
on single axis
and return

δy δx

δz

(b) Tilt sensitivity

Fixed focus,
specimen tilted

$T = 0$
$T = +\delta T$

Figure 3: Sensitivity of E_{eff} to *x*, *y* and *z* stage motions (a) and stage tilt (b). For the reload test in (a), the beam electron high tension (EHT) was switched off, chamber vented, and sample removed. The procedure was reversed to reload the sample.

4.3 Sensitivity to focus

Since the stage *z* axis was found to have the largest impact on strain noise, a full study of the effect of beam focus was performed to further understand the influence of sample *z* position and working distance. Here we define the working distance as the point of focus of the electron beam, controlled by the strength of the objective lens in the column. Physically, this is the narrowest point of the beam [9]. The *z* position is taken as in Section 4.2, i.e. the stage *z* coordinate.

For a fully aligned electron beam, where astigmatism and aperture alignment have been corrected, focus is achieved by bringing the focal point of the beam and the sample surface to a coincident height. This can be accomplished in two ways: by fixing the stage *z* coordinate and changing the working distance; or by fixing the beam working distance and bringing the sample into focus through changes in *z* position. Whilst these two methods

achieve the same goal, the sensitivity in strain noise may not be the same. There are also practical implications for automated testing and image acquisition. For example, the autofocus function within the Zeiss EVO 10 varies the working distance to optimise the focus with the specimen remaining stationary. However, the large area mapping function within the Oxford Instruments Aztec software uses a fixed working distance for the entire area mapped, interpolated between user defined stage coordinates where the user has focussed the microscope using only the stage *z*-coordinate due to a lack of automated column-based focus capability within this microscope. These subtly different capture processes may introduce different levels of strain noise.

To examine this, we attempted to separate out these two effects in a systematic way. For both studies, the specimen was brought to a reference working distance of 5.5 mm from the pole piece. The lenses were degaussed to remove any hysteresis. The image was then focussed with brightness and contrast optimised, and a reference image was captured.

For the first test, the working distance was varied in 1 μm increments whilst fixing the specimen position, recording images at each trial working distance. A range of 10 μm under and over focus were examined (Figure 4). For the second test, we performed the opposite experiment, fixing the working distance at 5.5 mm and displacing the stage in 1 μm increments over the same range, recording a new image at each increment (Figure 5).
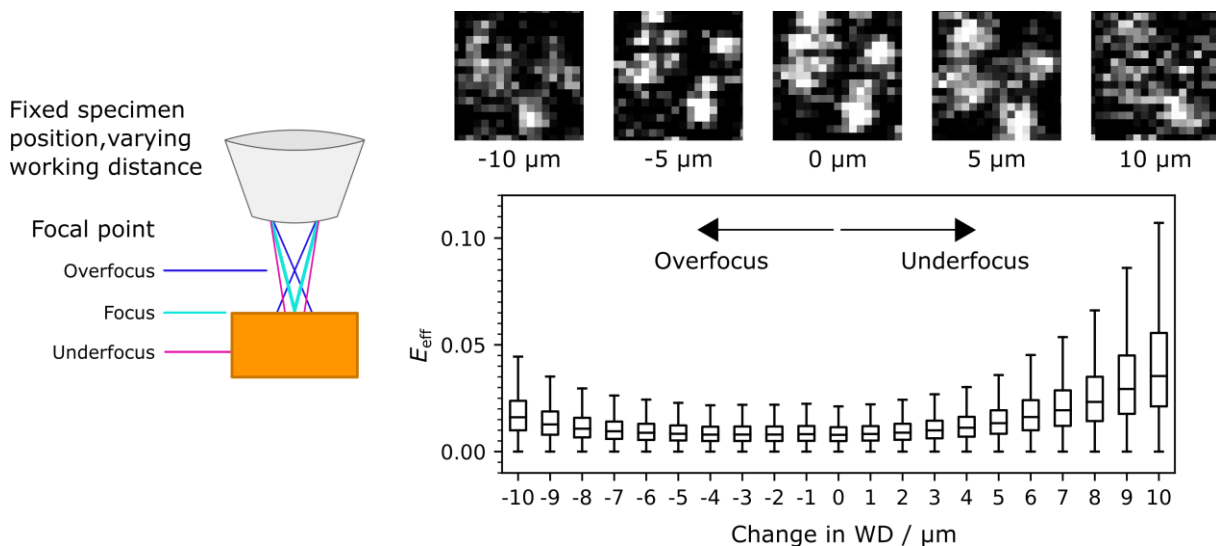
Figure 4: Noise sensitivity to working distance for fixed specimen position showing noise distributions as a function of working distance deviation and representative raw electron images at pixel resolution. Speckle images have a width of 300 nm.
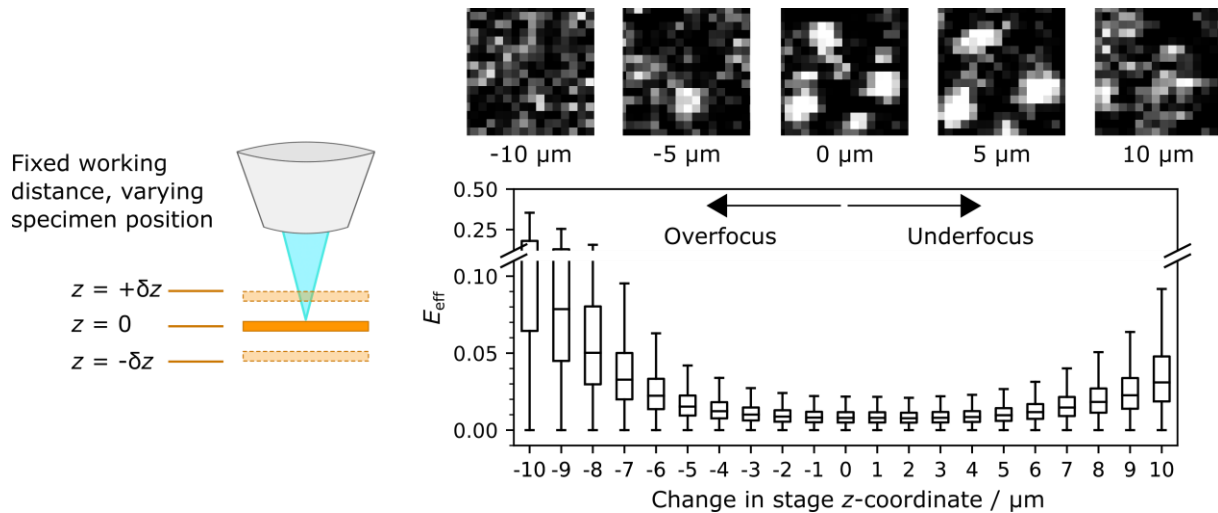
Figure 5: Noise sensitivity to specimen *z*-position for a fixed working distance showing noise distributions as a function of stage *z*-coordinate deviation and representative raw electron images at pixel resolution. Note the split y-axis due to large strain noise values for extreme negative stage *z*-coordinates. Speckle images have a width of 300 nm.

Both tests show a robustness to deviations in focus up to approximately 5 µm out of focus in both directions. This is a significant window in focus error which still gives tolerable levels of strain noise. Although there is clear degradation in the sharpness of individual speckles for a 5 µm focus error, the correlation was still successful and the strain noise remained less than 1% effective strain. Larger focus errors resulted in unacceptable levels of noise. As to whether these deviations in focus will prevent accurate analysis of deformed materials, studies using atomic force microscopy have found upper-bound out-of-plane displacements of 4 µm in deformed single crystals, with polycrystals showing levels of the order of 1 µm [18]. As such, the operating window here is robust for typical deformation studies.

We define an underfocussed beam as one where the working distance is greater than the distance between the specimen surface and the pole piece. The strain noise response for underfocus was identical for both tests resulting in a 3% strain value for 10 µm of focus deviation. This is because the two scenarios (altering the working distance and altering the specimen position) are effectively equivalent with a slight offset from one another, given that the absolute difference in working distances between the two is only several microns.

The most detrimental case for focus error is that due to overfocus caused by incorrect stage *z*-coordinates. In this example, we find a rapid degradation in strain measurement quality with the peak noise exceeding 40% for a -10 µm shift in specimen height. We believe that this is due to the increased physical distance between the specimen surface and backscatter detector, reducing the total signal reaching the detector. Inaccuracies in the stage positioning may also contribute to this, as assessed in Section 4.2.

4.4   Sensitivity to changes in magnification

Due to their scanning probe nature, there is some error in the measurement of distances using SEMs. The accuracy of both magnification and scale as reported by SEM software is a function of the accuracy of the beam control. Whilst SEMs may be regularly calibrated, the image scale reported can fluctuate over time. Mello et al. [2] have examined this, finding significant changes to reported distances measured using a silicon calibration specimen. They suggest the use of a known calibration sample, such as a silicon grid calibration

standard, to ensure that the magnification and scale are the same between imaging sessions. However, it is often not practical to recalibrate image scales during multistage in- or ex-situ deformation experiments. We therefore aim to characterise the sensitivity of measured strains to inaccuracies in scale and magnification.

We again take a reference image at 35 μm horizontal field width (HFW) prior to any perturbation. We then adjust the reported HFW by a set increment, recording a second image without any other changes to the microscope. Increments of ± 3 μm were chosen as this is significantly more than would be expected in an actual experiment and enables us to understand how to recognise this in a deformed dataset. For this study, we examine all components of the strain tensor as well as the effective strain as errors in magnification may introduce hydrostatic dilation of the images.
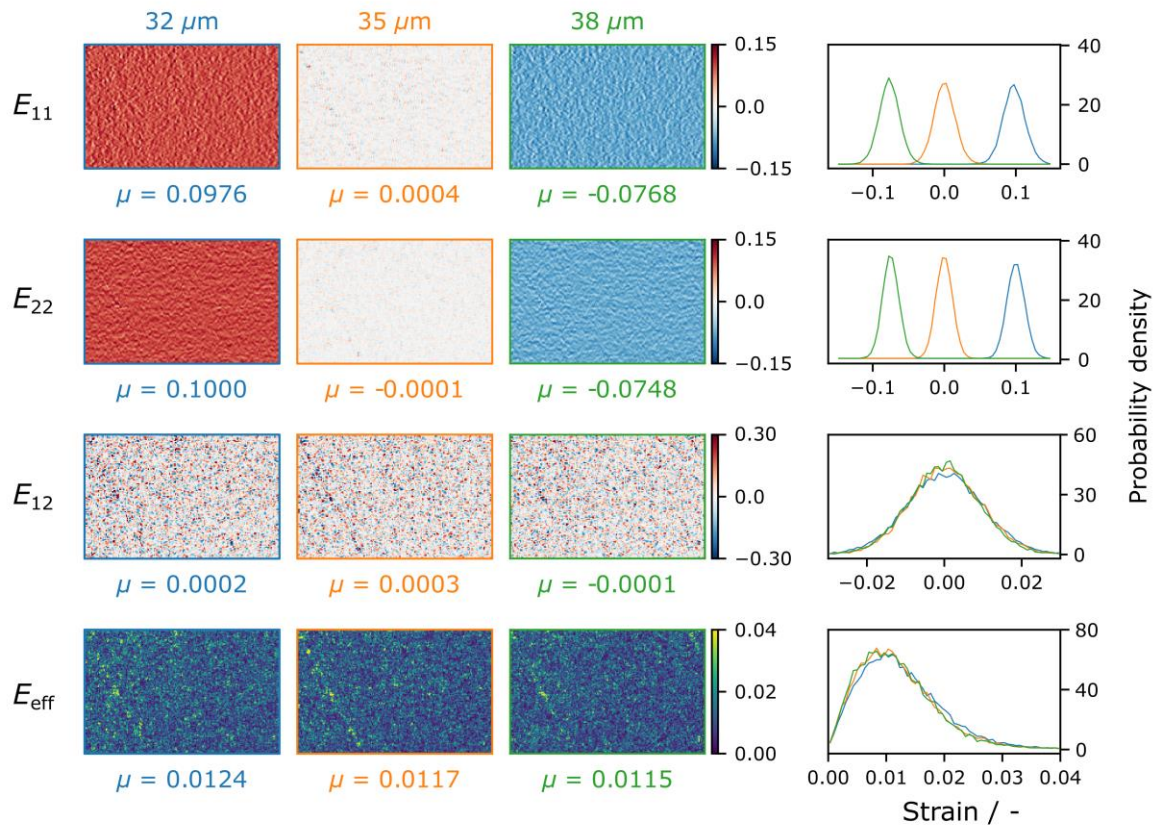

Figure 6: Full field strain maps showing the effect of HFW mismatch between correlated images. For all images, a 35 μm HFW reference image was used. Distributions for each strain component are given on the right with the curve colours corresponding to different test field widths (blue 32 μm, orange 35 μm, green 38 μm). Direction 1 is horizontal, 2 vertical. The diagonal feature in the shear maps is related to a grain boundary in the copper substrate. The linear feature visible in some of the maps is due to a slight change in image contrast at a grain boundary.

Intuitively, correlating an image with a smaller field of view than the reference image results in pure hydrostatic tension (Figure 6). Conversely, correlating a larger image against the reference image produces pure hydrostatic compression. In Figure 6 we show the effect of positive and negative HFW offsets of 3 μm. In both cases, the shift in the mean values of the 11 and 22 strain components match those expected due to the HFW offset. Direct strain components have a Gaussian distribution, shifted by the strain caused by the HFW mismatch.

The effective dilation of the images does not produce any shear deformation, and as such there are no changes to shear strain measures. Mean values of E_{12} are approximately zero

for all HFW images, with the mean values of the effective strain all at the acceptable noise level of 1%. Distributions of both shear strain measures are also unaffected by HFW changes. Figure 7 shows various strain measures for incremental changes in HFW. We observe a linear relationship between HFW mismatch and the 11 and 22 strain components, with shear strain measures insensitive to HFW mismatch.
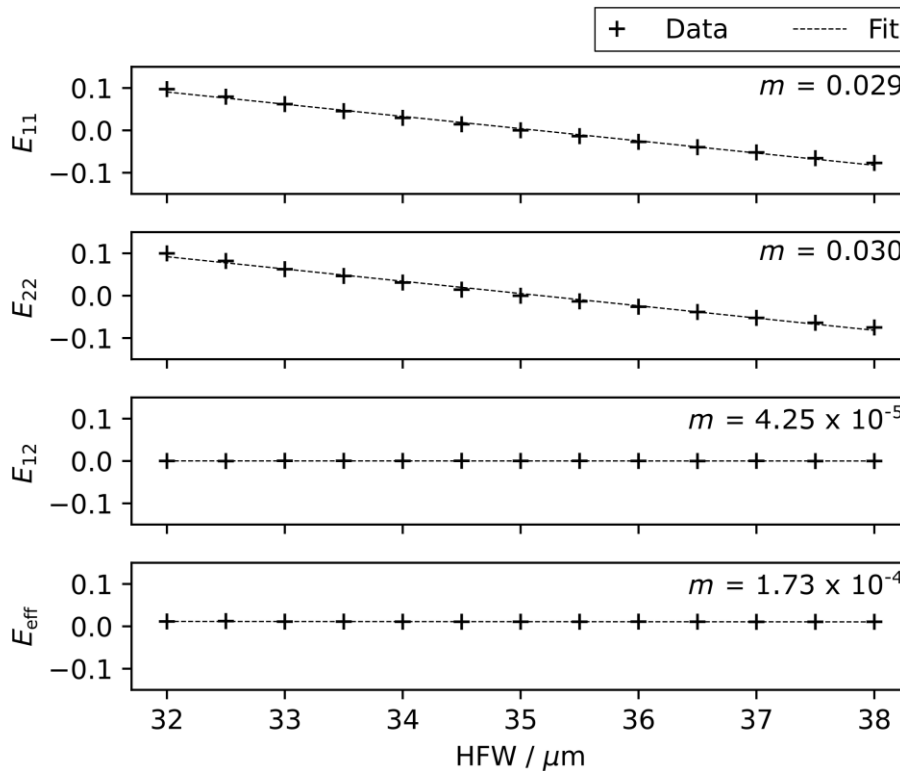
Figure 7: Median values of strain components as a function of test image HFW with gradients *m* of a linear fit. The reference image has a HFW of 35 µm. The examples in Figure 6 are the extremes of the data in this figure.

4.5 Recommended operating guidance of a LaB_6 SEM for HRDIC

The operating conditions described here were found to be the most optimal for this instrument, but we recommend that individual column, source, and detector configurations will likely need subtly different conditions. We offer the following guidance to optimise LaB_6 instruments for BSE imaging suitable for HRDIC:

- Cold filament starts should be avoided. The filament should be brought up to temperature and allowed to stabilise for approximately one hour or more to reduce any start-up instabilities in emission.
- Gun alignment is critical to success. The alignment of the gun should be performed when the filament is first started and repeated following the stabilisation period as any shift in the emission spot during imaging will affect the brightness and contrast of the resulting images.
- Gun vacuum hygiene must be maintained to ensure the level of beam stability for HRDIC is achieved. This necessitates regular gun bakeouts and general cleanliness of the instrument.
- When stability becomes unacceptable, we recommend removing the filament and thoroughly cleaning the Wehnelt and gun anode, then reassembling the gun with the filament's height reset to account for evaporation of the LaB_6 source.

- If gun cleaning does not solve the stability issue, we suggest replacing the filament. Whilst these partially spent filaments may still be suitable for general imaging, EBSD and x-ray analysis, their use for HRDIC may be limited.

It should be noted that although this study was performed using a LaB_6 source, we believe that a tungsten-source SEM would behave similarly due to the similarity between tungsten and LaB_6 filaments, with the penalty of reduced resolution and reduced filament lifetime.

4.6 Discussion

The errors in strain measurement quantified here represent a snapshot of the response of the Zeiss EVO 10 SEM for a given set of operating conditions. These studies demonstrate that a LaB_6 SEM is suitable for HRDIC strain measurement whilst also highlighting the robustness of this technique. However, a thorough understanding of the sensitivities of each microscope is required to better understand uncertainties in measurement and to best optimise imaging conditions. In these error analyses, inaccuracies in the horizontal stage positions and the effects of specimen removal and reloading are generally tolerable. This is promising for ex-situ experiments requiring specimen reloading and in-situ experiments using automation. These errors are relatively small when compared to those caused by inaccurate focus and magnification.

For these imaging conditions, focus deviations of up to 5 μm in either direction are acceptable, satisfying the 1% strain noise criterion. For the 5.5 mm working distance used here, this represents a 0.1% change in focus. Control of focus is therefore a key parameter for successful HRDIC measurement. Errors caused by beam inaccuracies are lower than those caused by stage inaccuracies. As such we recommend the use of focussing strategies controlling the electron lenses rather than the specimen position for any automated testing. Out-of-plane motion may be encountered during deformation, becoming more apparent at large applied strains. This effect can be countered to a reasonable extent by refocussing the images for each image capture step. However, if a single focal plane is used across a large, montaged region of interest (ROI), any significant deformation induced topology will introduce spatially varying errors.

Inaccurate and inconsistent magnification can introduce significant errors into measurement, particularly for low strains. This effect has several practical implications. The first is that shear strain measures are insensitive to this type of image distortion. Shear strain measures, either the effective strain or the traditional E_{12} strain measure, are often used to quantify strain in HRDIC when studying metallic systems (e.g. [11,13,19,20] but many other examples exist) as they better represent shear-type deformation mechanisms such as slip or grain boundary sliding. These strain measures are therefore more robust than other strain measures. The second implication is that all strain components should be examined when assessing the quality of HRDIC data. Examining shear maps in isolation may hide significant magnification errors within images. The final implication is that care must be taken to ensure consistency between imaging conditions. The magnitude of the fictitious direct strains is directly proportional to the HFW mismatch, i.e. a 1% change in apparent image width leads to 1% measured E_{11} and E_{22} strains. As such, extreme care must be taken if small strain values are of interest. Mello et al. [2] suggest the use of a silicon calibration specimen to quantify this error, finding approximately a 2% change in image width using identical imaging conditions on different days. We also recommend that users periodically check for changes in magnification over time and to carefully examine all strain components when analysing strain data.

5   CASE-STUDY IN OFHC-CU

OFHC-Cu (99.99% purity, 0.0005% maximum oxygen, City Special Metals Ltd.) was selected for this case study due to its small 30 μm grain size giving a large number of grains within a practical region of interest.


5.1   Specimen preparation, patterning and testing

5.1.1 Material Characterisation

Tensile dogbone specimens were electric-discharge machined from a larger plate of OFHC-Cu. The EDM recast layer was removed from both sides of the specimen resulting in a specimen approximately 1.2 mm thick. The front face was prepared using the method described in [14] to leave a surface suitable for patterning and EBSD analysis.

Fiducial microhardness indents (~40 μm width) were used to mark the region of interest and allow easy reacquisition during the various microscopy steps during the experiment. These were placed approximately 1 mm away from the ROI to ensure that the strain field caused by the indents did not influence the deformation of the ROI. Kernel average misorientation measurements from pre-deformation EBSD mapping showed no influence of the fiducial hardness indents. Stage coordinates were then used to locate the ROI, using the indents as an origin on the specimen. The specimen edge was used to align the specimen within the microscope.

Pre-deformation EBSD mapping was performed on a 500 μm × 400 μm area containing approximately 500 grains to sample a range of microstructural features including a variety of grain sizes, morphologies and annealing twins. A Zeiss EVO 10 LaB$_6$ SEM with an Oxford Instruments Symmetry EBSD camera was used for all EBSD analysis with the following parameters: 20 kV accelerating voltage, 10 nA beam current, 30 μm aperture, 200 nm step size. The central 400 μm × 300 μm region of this map was taken as the ROI, shown in Figure 8. This region contains a range of grain sizes, orientations and morphologies, with a significant number of annealing twins, providing a statistical representation of the deformation modes expected across the sample.
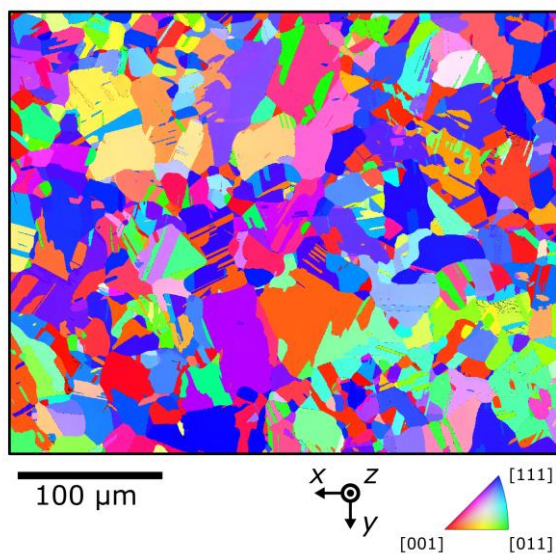

Figure 8: Orientation map of the region of interest. Orientations shown are parallel to the *x*-direction, which is the tensile loading axis used in this study. The indexing hit rate here is 99.4%. No data cleaning is applied.

Following EBSD the specimen was patterned as described in [14]. A 3 nm layer of titanium was first deposited on the surface, followed by 5 nm of silver. The pattern was remodelled with a 1 wt.% NaBr solution in isopropanol for 120 minutes, resulting in speckles approximately 50 – 80 nm in diameter and 20% surface coverage.

5.1.2 Image acquisition and HRDIC noise assessment

BSE images for HRDIC were recorded with the same Zeiss EVO 10 SEM with 20 kV accelerating voltage, 1 nA beam current, 20 µm aperture using a four diode, and a pole-piece mounted backscatter detector. Individual 35 µm images with 2048 × 1536 pixel store resolution were recorded in a mosaic covering the ROI. A 10-µs dwell time resulted in a frame capture time of ~35 s. A 20% image overlap was used to ensure full coverage and successful image stitching by accounting for the effect of tensile deformation. Image collection was controlled with the Oxford Instruments Aztec software montage capability. Focus was controlled with the stage z-coordinate with a fixed working distance, driving the stage to focus in the four corners and the software interpolating stage height in between. The image matrix for each strain step took approximately three hours to capture.

The noise measurements detailed in Section 4 were all taken in the non-deformed state, correlating pairs of images taken sequentially without any applied deformation. In real experiments, deformation will affect the specimen surface, which may affect the strain measurement noise floor. Slip steps, grain boundary sliding and out-of-plane grain rotation will all introduce surface topology changes as a function of deformation. Unlike the instrument parameters examined in Section 4, these changes cannot be controlled. As such, we wish to quantify their effect on strain noise to provide a better estimate on uncertainty in measurement. Following each imaging step, a second 3 × 3 grid of images were captured in the upper left of the ROI, using identical parameters to the main imaging step. These images were used to quantify the effect of applied deformation on the noise floor. The full imaging procedure is shown schematically in Figure 9.
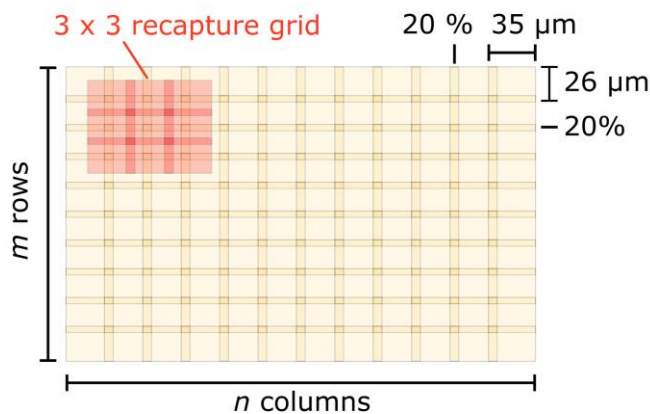
Figure 9: Image capture sequence showing the main imaging grid and the additional noise measurement imaging grid.

5.1.3 Mechanical Loading

Specimens were deformed in tension ex-situ under displacement control with a 10 kN capacity Instron 5966 testing machine. Specimens were loaded at the shoulders using grips with alignment pins to ensure only in-plane motion without twisting. Testing was interrupted at nominally 1.0% and 1.5% plastic strain by applying the corresponding crosshead displacements to achieve these strains, with a nominal strain rate of 1×10^{-3} s^{-1}. Engineering stress-strain curves are presented in Figure 10 for the two deformation cycles. The specimen was removed from the testing machine for imaging in the SEM. The actual strains in the ROI were calculated by taking the average values of the strains measured using HRDIC.
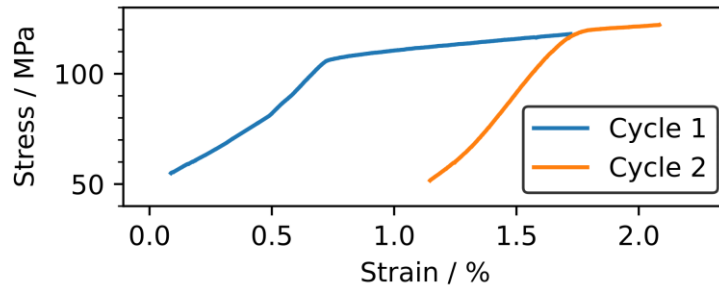
Figure 10: Engineering stress – strain curves for the two deformation cycles, calculated using force and crosshead displacement data.

Grids of images for each deformation step were stitched together using the Grid/Collection Stitching tool within ImageJ [21]. Individual image arrays were approximately 500 megabytes in size. LaVision DaVis 10.0.5 was used to perform the image correlation, first performing a shift and rotation correction to remove any small rigid body motion between images followed by an FFT-based cross-correlation algorithm with a reducing window size using the optimised parameters shown previously. The resulting spatial resolution of the strain measurements was 136 nm. The DefDAP python package (v0.93) was used to register HRDIC displacement and EBSD orientation maps, to calculate the strain fields, and for all data post processing [16]. Manually placed control points were used to register the EBSD and HRDIC datasets, using a projective transform to correct for EBSD distortions [17]. Error analysis was performed using in-house python scripts.

5.2   Results and discussion

5.2.1 Effect of deformation on noise

Here, we look at strains just beyond the macroscopic yield but further assessment of these errors is required to higher plastic strains. In this study, the strain noise appeared to have no dependence on applied deformation. Since we examine a 3×3 image grid, these measurements include the effect of image stitching, inherent in large-area mapping experiments. All strain components showed no change in median noise level or noise distribution following deformation (Figure 11). All strain maps fulfilled our 1% effective strain noise floor criterion. The absence of any change in the 11 and 22 strain components demonstrates stability in image magnification between deformation steps discussed in Section 4.4.
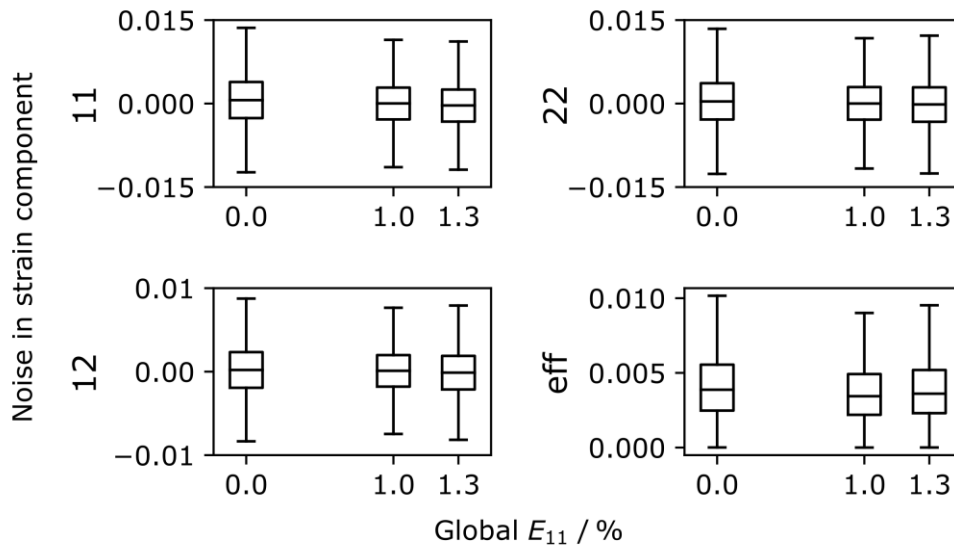
Figure 11: Measured noise in strain components as a function of the global applied tensile strain. The strain distributions here are calculated from the small subregion shown in Figure 9, with the global E_{11} values calculated by taking the average values for the entire ROI.

5.2.2 Strain Mapping in OFHC-Cu

The full-field displacement data are represented as maps of effective shear strain in Figure 12 with the grain boundaries overlaid to show the nature of the strain localisation relative to the underlying microstructure. Strain maps are shown for 1.0% and 1.3% average plastic strain in the loading direction and show highly heterogeneous strain patterns (Figure 12a and b, respectively). Discrepancies between the HRDIC-measured average strain values and those applied with crosshead displacement are due to compliance in the load chain. Due to the single-phase nature of this copper, with no alloying additions, one would expect relatively uniform deformation behaviour across the entire map. In other metallic systems, a single slip character generally dominates, for example, fine planar slip [12] and grain boundary localisation [10] in magnesium, well separated planar slip in austenitic steels [22,23], or diffuse, homogenous slip in in zirconium [24]. Nickel-base superalloys exhibit complex slip behaviour [19,25] but the presence of γ′-precipitates influences the slip character. Since the OFHC-Cu is devoid of any low-length scale microstructural features, the complexity of the slip character is surprising.
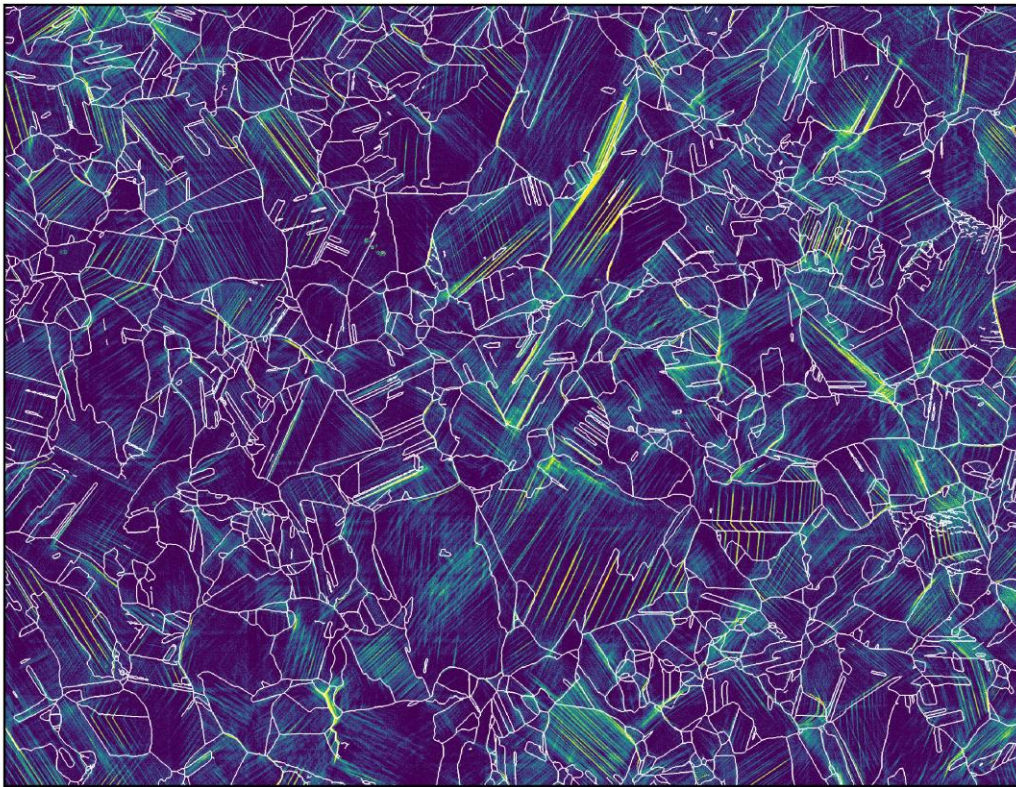
(a) Cycle 1, $\bar{E}_{11} = 1.0$ %
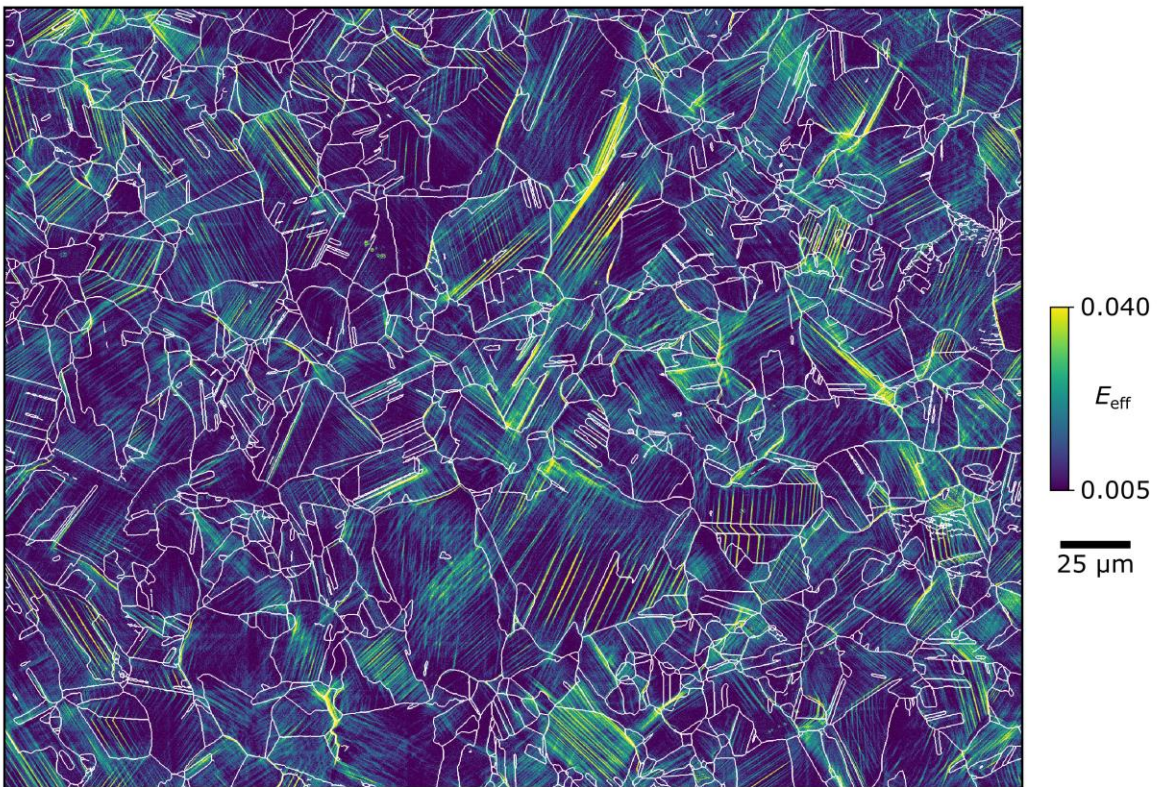
(b) Cycle 2, $\bar{E}_{11} = 1.3$ %

Figure 12: Maps of effective strain for the ROI for each deformation cycle, using a strain subset size of 16 px and an overlap of 50% giving a spatial resolution of 140 nm. Grain boundaries from the pre-deformation a EBSD scan are overlaid in white. Specimens were loaded in tension in the horizontal direction.

The trends in slip patterning begin early in the deformation process, and in this case appear to be fully developed after the first deformation cycle. The intensity of all deformation features increased following a second deformation cycle but there appeared to be no new deformation structures. Grain boundaries showing localisation after cycle 1 continued to deform but no new examples of grain boundary localisation were observed. Grains showing higher levels of deformation continued to deform further with increasing applied strain but there were no significant changes in the overall patterns. This is due to the small increment in deformation between the two steps. At larger strains, it would be expected that new slip bands would be necessary to accommodate deformation due to the saturation of existing dislocation structures [26].

Four characteristic deformation behaviours observed from the strain maps have been highlighted in Figure 13, referred to as planar single slip, grain boundary strain localisation, interacting diffuse slip bands, and multiple slip activation within single grains. These four mechanisms are found at various locations within the ROI with no single mechanism dominating.

Several grains exhibit widely spaced, intense slip bands. This behaviour appears to correlate with higher levels of slip transfer across grain boundaries. Figure 13a shows highly discrete slip bands within a larger, twinned grain, with high levels of slip transmission. For the grain to accommodate a given amount of applied deformation with fewer active slip bands, the intensity of deformation along each slip band must be greater. This causes a high level of stress concentration where the slip band meets the grain boundary, increasing the likelihood of nucleating a new slip band in the neighbouring grain. For diffuse slip, this stress concentration effect is diminished, reducing the likelihood of slip transfer.
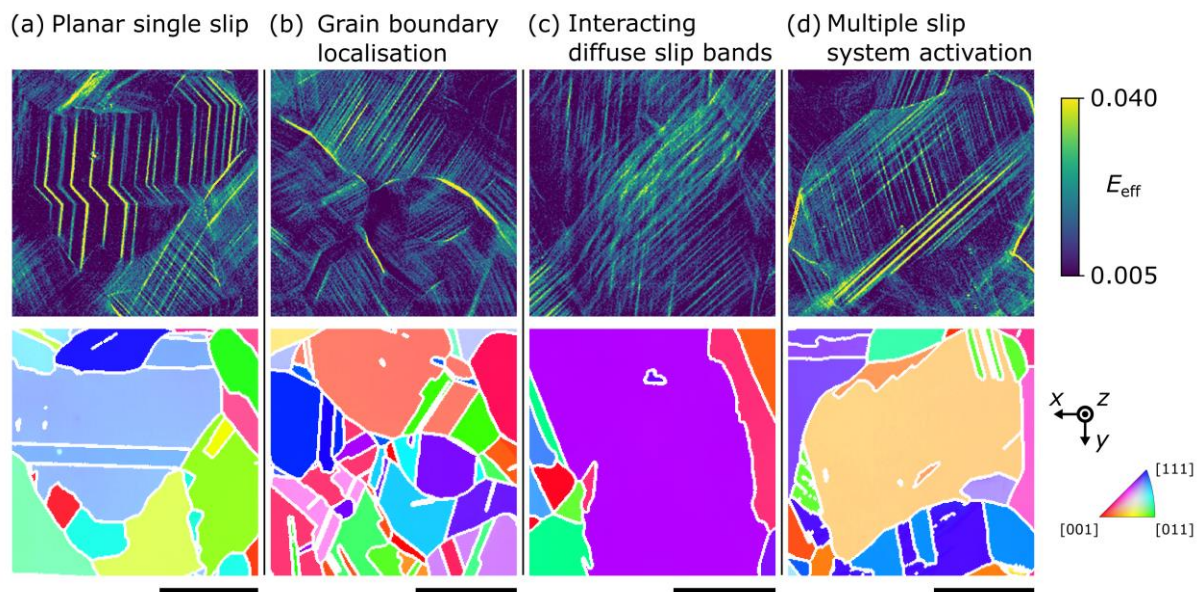
Figure 13: Detail of various slip behaviour observed within the ROI, with corresponding orientation maps. Orientations shown are with respect to the sample *x*-direction. Strain maps are those following cycle 2, with a mean *x*-strain of 1.3%. The scale bar for each column is 20 μm.

Significant grain boundary strain localisation is observed across the ROI (Figure 13b). Grain boundary sliding is known to be a key mechanism contributing to the poor creep performance of pure copper, with continued grain boundary sliding leading to the formation of cavities [27–29]. The observation of significant grain boundary sliding in this room temperature study at low applied deformation is consistent with the literature.

Significant regions of diffuse slip, containing tightly spaced, indistinct slip bands, are found in many grains throughout the ROI. Many of these regions are the result of two simultaneously active slip systems (Figure 13c). This is generally found within larger grains where there is sufficient stress heterogeneity across the grain to activate multiple slip systems. This diffuse slip is unlikely to be a result of cross-slip however, due to the relatively low stacking fault energy of copper [30,31].

Finally, numerous grains display the activation of multiple slip systems (Figure 13d). In some grains, this manifests itself as packets of overlapping slip traces, whereas other grains display grain segmentation with different slip traces dominating in different sections of the grain. Grain segmentation due to heterogeneous slip activation has been observed in other polycrystals, with dissimilar slip system activation across a given grain requiring significant lattice rotation to maintain compatibility [22,24]. For overlapping slip traces, the maximum strain is associated with the point slip trace intersection. This is concordant with similar findings in austenitic steel where slip band interaction is accompanied by the generation of geometrically necessary dislocations [23]. Both multiple slip activation mechanisms observed here will contribute to work hardening.

Further study into the deformation behaviour of pure copper and copper-base alloys using full field, microstructural strain mapping is necessary, but is beyond the scope of the study presented here. However, we have demonstrated the ability to qualitatively identify the primary deformation mechanisms in deformed materials when using a LaB_6 SEM for HRDIC. The following section will demonstrate quantitative accuracy via slip system identification.

5.2.3 Slip system identification

There is a need to understand slip system activity in these deformation studies, in particular if we wish to construct explicitly representative crystal plasticity models based on these experimental data. As such, unambiguous identification of slip system activation is required. The strain maps presented here are of sufficient resolution to readily perform slip trace analysis, as slip traces can be clearly resolved and orientation data can be easily linked. However, slip trace analysis is ambiguous and calculating a grain's Schmid factor using the global stress state can lead to the misidentification of active slip systems due to fluctuations in local stress states [23]. It is therefore more useful to determine the active slip system uniquely by using conventional slip trace analysis to determine the slip plane and by then finding the slip system Burger's vector direction using the relative displacement ratio (RDR) method [8]. This method utilises the displacement data and accordingly requires high quality data. This analysis technique thus represents a critical assessment of whether the data generated from a LaB_6 SEM is of sufficient quality for HRDIC.

A selection of grains were selected from the strain map, Figure 12, to assess the suitability of the data for applying the RDR method. Grains were chosen so that a variation of deformation behaviour was sampled, including: (i) grains with distinct, well separated bands; (ii) diffuse slip; and (iii) closely packed slip bands. Three slip bands within each example grain were used in the RDR calculation. A five-pixel perpendicular sample line was taken across each measured slip band, centred symmetrically on the band to provide displacements either side of the inter slip trace region. Candidate slip traces were compared with those predicted from grain orientations with an acceptable criterion of ±5°. For the copper examined here, slip is only possible on the $\{111\} < 1\bar{1}0 >$ type slip systems, giving four possible slip traces, each with three possible Burgers vectors. Figure 14 shows the selected grains and the RDR correlation graphs, with Table 1 detailing the calculated and experimentally measured RDR values and slip trace angles. Schmid factors are calculated by assuming that the global tensile stress state in the horizontal (x) direction is representative for all grains.

Grain 1 represents a simple case of parallel, well-spaced high intensity slip bands with a single slip trace within the grain. This grain is the parent of a larger grain containing an

annealing twin. The three highest intensity slip bands were used in the RDR calculation. The (111) plane is easily identified as active from slip trace analysis with the slip direction unambiguously determined to be [$\bar{1}$01].

Grain 2 also contains a single set of parallel slip traces. However, slip identification is more challenging than in Grain 1 due to the close spacing of the slip traces. The active slip plane is easily identified as ($\bar{1}$11) with RDR analysis determining the active slip system as [$\bar{1}\bar{1}$0]. The high correlation coefficient (0.91) and small deviation between calculated and experimentally measured RDR values provides confidence in the validity of the slip system identification. This analysis also allows us to discriminate between two high Schmid factor slip directions on the ($\bar{1}$11) plane. This demonstrates the difficulty of using traditional global Schmid factor analysis, especially where apparent Schmid factors are close. In this situation, small deviations in local stress state become critical in determining the active slip system. For the grain analysed here, the slip system with the second highest global Schmid factor is in fact active, emphasising the effect of microstructure on local stress states.

Grain 3 shows low intensity slip bands with two groups of slip trace directions within the grain. One of these slip trace directions has been chosen for the RDR analysis. For the selected slip trace, there are two candidate theoretical slip planes, one satisfying the ±5°criterion and the other falling slightly outside of this. The associated slip planes both contain Burgers vectors with Schmid factors greater than 0.4, which means it is highly favourable for slip. Whilst there is more noise than Grains 1 and 2 in the centred *u* and *v* displacement values, a RDR value can be successfully extracted ($RDR_{\mathrm{exp}} = 2.40$). This unambiguously correlates with the active slip system ($RDR = 2.81$) that falls within the angle criterion. The high global Schmid factor slip system for the plane that was outside of the angle criterion did not match, having an RDR value of 4.30.

The grains analysed in detail demonstrate the data generated here is of sufficient quality to enable full slip system identification for a range of different deformation behaviours. Other grains within these strain maps have also been successfully analysed, provided that discrete slip bands were visible. As such, we can be confident that the full-field strain data produced by LaB$_6$ SEMs is comparable to that generated using FESEM systems.
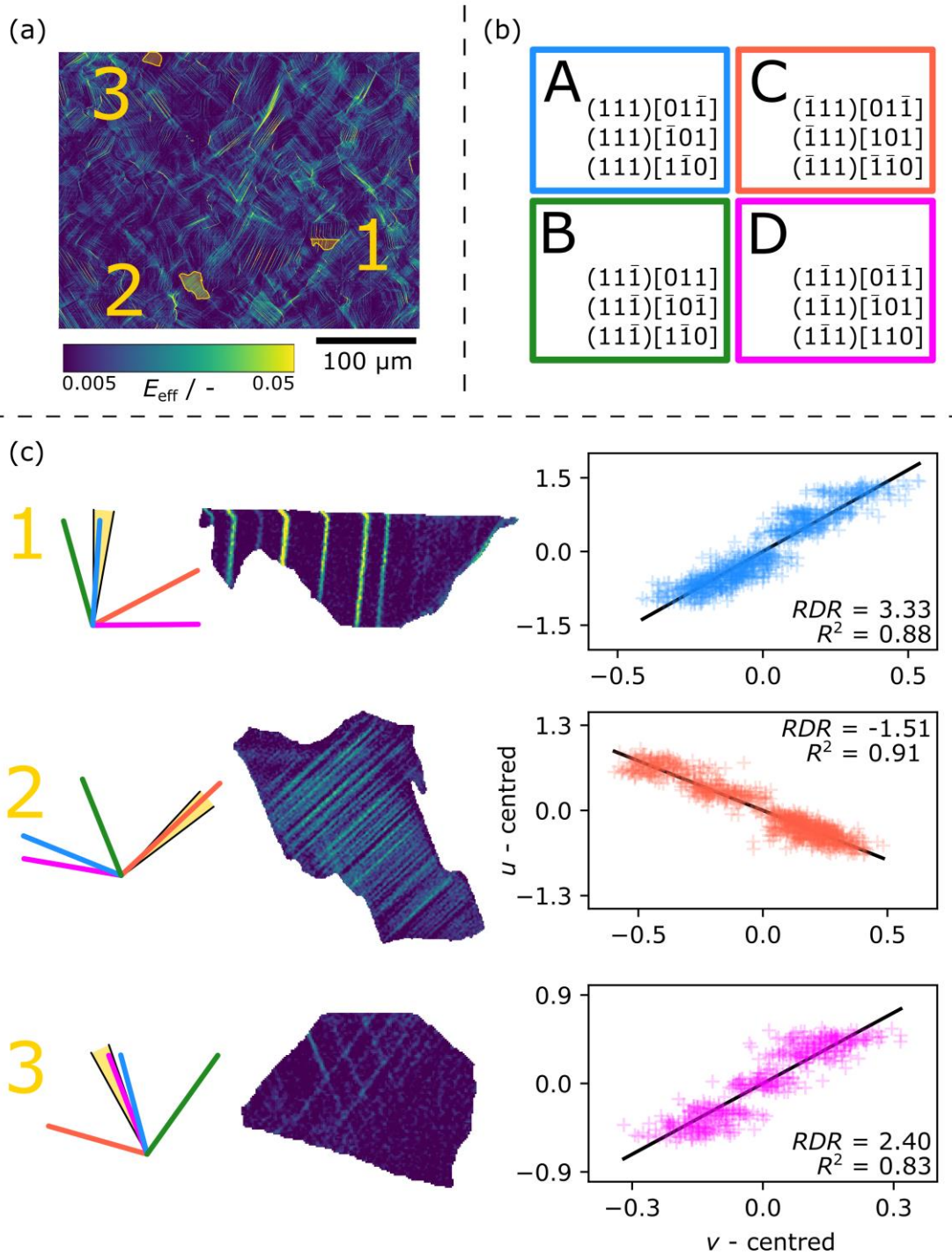
Figure 14: RDR analysis for three chosen grains from the larger strain map (a). Twelve $\{111\} < 1\bar{1}0 >$ slip systems are considered for analysis (b). For each grain, we compare experimental slip traces to the possible traces as determined by grain orientations. Plots of the *u* and *v* shifts across the slip traces and performing a linear regression allows us to determine the RDR values (c).

Table 1: RDR analysis for the three grains selected in Figure 14. Candidate slip planes are selected by comparing the measured slip trace angle θ_{exp} with the angle predicted from the grain orientation θ_{calc}. Theoretical RDR values (RDR_{calc}) are then calculated for all possible slip directions and compared with the experimentally measured value RDR_{exp}. Schmid factors (*M*) are calculated using the global horizontal tensile loading stress state. Grain 3 contains two similarly oriented slip traces; only the slip trace on plane D are assessed here.

Grain	Candidate slip plane	direction	RDR_{calc}	M	RDR_{exp}	θ_{calc}	θ_{exp}
1	A (111)	$[01\bar{1}]$	-0.77	0.34			
		$[\bar{1}01]$	**3.36**	**0.47**	**3.33**	**174.9**	**174.9**
		$[110]$	0.21	0.13			
2	C ($\bar{1}11$)	$[01\bar{1}]$	-0.91	0.44			
		$[101]$	-0.03	0.01			
		$[\bar{1}\bar{1}0]$	**-1.60**	**0.43**	**-1.51**	**133.6**	**132.1**
3	A (111)	$[01\bar{1}]$	4.30	0.40			
		$[\bar{1}01]$	0.35	0.15		15.8	
		$[110]$	-0.74	0.25			
	D ($1\bar{1}1$)	$[0\bar{1}\bar{1}]$	-0.67	0.28			
		$[\bar{1}01]$	0.35	0.21			
		$[\mathbf{110}]$	**2.81**	**0.49**	**2.40**	**21.6**	**24.4**

6   CONCLUSION

We have validated the use of LaB$_6$ source SEMs as a viable tool for HRDIC-based strain mapping, achieving results typical of field emission source SEMs. The noise response of our instrument has been characterised, examining the effect of various system parameters. We found that control of focus and magnification are key to minimising strain errors in experiments, outweighing the effects of stage accuracy. This demonstrates that ex-situ experiments requiring sample reloads and any experiment relying on automation of stage position for large area mapping should not be subject to unacceptable strain noise due to stage accuracy. Focus using the electron optics offers a superior operating window when compared to that achieved using stage *z*-coordinate to focus. Control of magnification is crucial in reducing the presence of fictitious hydrostatic strains. However, the use of shear type strain measures, including our favoured maximum in-plane shear strain, is robust to this effect whilst also capturing the primary deformation characteristics of metal plasticity at the microscale.

We present a case study using a material relevant for application in nuclear fusion technology, oxygen-free high-conductivity copper, deformed ex-situ with two loading cycles to a maximum applied strain of 1.3%. Noise in the full field strain data was quantified as a function of applied global strain and found to be acceptable throughout the experiment. In this study, we observe a range of deformation mechanisms including planar slip, multiple slip system activation and interaction within single grains, diffuse slip, and grain boundary strain localisation. This reveals the complexity of deformation behaviour in a relatively simple, single-phase microstructure whilst highlighting the quality of results produced with a LaB$_6$ SEM. Relative displacement ratio characterisation was successfully used to determine the active slip system in a range of grains with different slip characteristics. The observation of these characteristic deformation behaviours as well as the ability to extract active slip

systems from the strain maps provides insight necessary to build representative crystal plasticity models to predict the performance of these materials in the challenging fusion environment. The success of this study also demonstrates the utility of conventional, non-field emission SEM instruments in the capture of high-quality strain mapping data, expanding the accessibility of this technique to the wider strain measurement community.

7   ACKNOWLEDGEMENTS

8   REFERENCES

[1]   International Digital Image Correlation Society, E. Jones, M. Iadicola, R. Bigger, B. Blaysat, C. Boo, M. Grewer, J. Hu, A. Jones, M. Klein, K. Raghavan, P. Reu, T. Schmidt, T. Siebert, M. Simenson, D. Turner, A. Vieira, T. Weikert, A Good Practices Guide for Digital Image Correlation, 1st ed., International Digital Image Correlation Society, 2018. https://doi.org/10.32720/idics/gpg.ed1.

[2]   A.W. Mello, T.A. Book, A. Nicolas, S.E. Otto, C.J. Gilpin, M.D. Sangid, Distortion Correction Protocol for Digital Image Correlation after Scanning Electron Microscopy: Emphasis on Long Duration and Ex-Situ Experiments, Exp. Mech. 57 (2017) 1395–1409. https://doi.org/10.1007/s11340-017-0303-1.

[3]   S. Maraghechi, J.P.M. Hoefnagels, R.H.J. Peerlings, M.G.D. Geers, Correction of scan line shift artifacts in scanning electron microscopy: An extended digital image correlation framework, Ultramicroscopy. 187 (2018) 144–163. https://doi.org/10.1016/j.ultramic.2018.01.002.

[4]   S. Maraghechi, J.P.M. Hoefnagels, R.H.J. Peerlings, O. Rokoš, M.G.D. Geers, Correction of Scanning Electron Microscope Imaging Artifacts in a Novel Digital Image Correlation Framework, Exp. Mech. 59 (2019) 489–516. https://doi.org/10.1007/s11340-018-00469-w.

[5]   A.D. Kammers, S. Daly, Digital Image Correlation under Scanning Electron Microscopy: Methodology and Validation, Exp. Mech. 53 (2013) 1743–1761. https://doi.org/10.1007/s11340-013-9782-x.

[6]   W.C. Lenthe, J.C. Stinville, M.P. Echlin, Z. Chen, S. Daly, T.M. Pollock, Advanced detector signal acquisition and electron beam scanning for high resolution SEM imaging, Ultramicroscopy. 195 (2018) 93–100. https://doi.org/10.1016/j.ultramic.2018.08.025.

[7]   Z. Chen, W. Lenthe, J.C. Stinville, M. Echlin, T.M. Pollock, S. Daly, High-Resolution Deformation Mapping Across Large Fields of View Using Scanning Electron Microscopy and Digital Image Correlation, Exp. Mech. 58 (2018) 1407–1421. https://doi.org/10.1007/s11340-018-0419-y.

[8]   Z. Chen, S.H. Daly, Active Slip System Identification in Polycrystalline Metals by Digital Image Correlation (DIC), Exp. Mech. 57 (2017) 115–127. https://doi.org/10.1007/s11340-016-0217-3.

[9]   J.I. Goldstein, D.E. Newbury, P. Echlin, D.C. Joy, C.E. Lyman, E. Lifshin, L. Sawyer, J.R. Michael, Scanning Electron Microscopy and X-ray Microanalysis, Springer US, Boston, MA, 2003. https://doi.org/10.1007/978-1-4615-0215-9.

[10] B. Yavuzyegit, E. Avcu, A.D. Smith, J. Donoghue, D. Lunt, J.D. Robson, T.L. Burnett, J. Quinta da Fonseca, P.J. Withers, Mapping Plastic Deformation Mechanisms in AZ31 Magnesium Alloy at the Nanoscale, (2022). https://doi.org/10.2139/ssrn.4198880.

[11] D. Lunt, A. Orozco-Caballero, R. Thomas, P. Honniball, P. Frankel, M. Preuss, J. Quinta da Fonseca, Enabling high resolution strain mapping in zirconium alloys, Mater. Charact. 139 (2018) 355–363. https://doi.org/10.1016/j.matchar.2018.03.014.

[12] A. Orozco-Caballero, D. Lunt, J.D. Robson, J. Quinta da Fonseca, How magnesium accommodates local deformation incompatibility: A high-resolution digital image correlation study, Acta Mater. 133 (2017) 367–379. https://doi.org/10.1016/j.actamat.2017.05.040.

[13] F. Di Gioacchino, J. Quinta da Fonseca, Plastic Strain Mapping with Sub-micron Resolution Using Digital Image Correlation, Exp. Mech. 53 (2013) 743–754. https://doi.org/10.1007/s11340-012-9685-2.

[14] B. Poole, A. Marsh, D. Lunt, C. Hardie, M. Gorley, C. Hamelin, A. Harte, Nanoscale speckle patterning for high resolution strain mapping in fusion relevant Cu-base alloys, Strain - Rev. (n.d.).

[15] D. Lunt, R. Thomas, M. Roy, J. Duff, M. Atkinson, P. Frankel, M. Preuss, J. Quinta da Fonseca, Comparison of sub-grain scale digital image correlation calculated using commercial and open-source software packages, Mater. Charact. 163 (2020) 110271. https://doi.org/10.1016/j.matchar.2020.110271.

[16] M.D. Atkinson, R. Thomas, A. Harte, P. Crowther, J. Quinta da Fonseca, DefDAP: Deformation Data Analysis in Python - v0.92, (2020). https://doi.org/10.5281/zenodo.3784775.

[17] M.D. Atkinson, J.M. Donoghue, J.Q. da Fonseca, Measurement of local plastic strain during uniaxial reversed loading of nickel alloy 625, Mater. Charact. 168 (2020) 110561. https://doi.org/10.1016/j.matchar.2020.110561.

[18] L. Cretegny, A. Saxena, AFM characterization of the evolution of surface deformation during fatigue in polycrystalline copper, Acta Mater. 49 (2001) 3755–3765. https://doi.org/10.1016/S1359-6454(01)00271-3.

[19] A. Harte, M. Atkinson, M. Preuss, J. Quinta da Fonseca, A statistical study of the relationship between plastic strain and lattice misorientation on the surface of a deformed Ni-based superalloy, Acta Mater. 195 (2020) 555–570. https://doi.org/10.1016/j.actamat.2020.05.029.

[20] M.A. Linne, T.R. Bieler, S. Daly, The effect of microstructure on the relationship between grain boundary sliding and slip transmission in high purity aluminum, Int. J. Plast. 135 (2020) 102818. https://doi.org/10.1016/j.ijplas.2020.102818.

[21] S. Preibisch, S. Saalfeld, P. Tomancak, Globally optimal stitching of tiled 3D microscopic image acquisitions, Bioinformatics. 25 (2009) 1463–1465. https://doi.org/10.1093/bioinformatics/btp184.

[22] F. Di Gioacchino, J. Quinta da Fonseca, An experimental study of the polycrystalline plasticity of austenitic stainless steel, Int. J. Plast. 74 (2015) 92–109. https://doi.org/10.1016/j.ijplas.2015.05.012.

[23] B. Poole, F.P.E. Dunne, Slip band interactions and GND latent hardening in a galling resistant stainless steel, Mater. Sci. Eng. A. 813 (2021) 141176. https://doi.org/10.1016/j.msea.2021.141176.

[24] R. Thomas, D. Lunt, M.D. Atkinson, J. Quinta da Fonseca, M. Preuss, F. Barton, J. O'Hanlon, P. Frankel, Characterisation of irradiation enhanced strain localisation in a zirconium alloy, Materialia. 5 (2019) 100248. https://doi.org/10.1016/j.mtla.2019.100248.

[25] A. Harte, M. Atkinson, A. Smith, C. Drouven, S. Zaefferer, J. Quinta da Fonseca, M. Preuss, The effect of solid solution and gamma prime on the deformation modes in Ni-based superalloys, Acta Mater. 194 (2020) 257–275. https://doi.org/10.1016/j.actamat.2020.04.004.

[26] D.E. Kramer, M.F. Savage, L.E. Levine, AFM observations of slip band development in Al single crystals, Acta Mater. 53 (2005) 4655–4664. https://doi.org/10.1016/j.actamat.2005.06.019.

[27] R. Sandström, J. Hallgren, The role of creep in stress strain curves for copper, J. Nucl. Mater. 422 (2012) 51–57. https://doi.org/10.1016/j.jnucmat.2011.12.012.

[28] R. Sandström, R. Wu, J. Hagström, Grain boundary sliding in copper and its relation to cavity formation during creep, Mater. Sci. Eng. A. 651 (2016) 259–268. https://doi.org/10.1016/j.msea.2015.10.100.

[29] B. Wilshire, A.J. Battenbough, Creep and creep fracture of polycrystalline copper, Mater. Sci. Eng. A. 443 (2007) 156–166. https://doi.org/10.1016/j.msea.2006.08.094.

[30] U.F. Kocks, H. Mecking, Physics and phenomenology of strain hardening: the FCC case, Prog. Mater. Sci. 48 (2003) 171–273. https://doi.org/10.1016/S0079-6425(02)00003-8.

[31] F. Hamdi, S. Asgari, Influence of stacking fault energy and short-range ordering on dynamic recovery and work hardening behavior of copper alloys, Scr. Mater. - Scr. MATER. 62 (2010) 693–696. https://doi.org/10.1016/j.scriptamat.2010.01.031.